Nonlinear waveform and delay time analysis of triplicated core phases

R. Garcia

Département de Géophysique Spatiale et Planétaire, Institut de Physique du Globe de Paris, CNRS UMR7096, St. Maur des Fossés, France

S. Chevrot

Laboratoire de Dynamique Terrestre et Planétaire, CNRS UMR5562, Toulouse, France

M. Weber

GeoForschungsZentrum, Potsdam, Germany

Received 4 February 2003; revised 14 August 2003; accepted 29 August 2003; published 24 January 2004.

[1] We introduce a new method to measure differential travel times and attenuation of seismic body waves. The problem is formulated as a nonlinear inverse problem, which is solved by simulated annealing. Using this technique, we have analyzed triplicated *PKP* waves recorded by the temporary Eifel array in central Europe. These examples demonstrate the potential of the technique, which is able to determine differential travel times and waveforms of the core phases, even when they interfere on the seismograms or when additional depth phases are present. The *PKP* differential travel times reveal the presence of large-amplitude and small-scale heterogeneities along the *PKP*(AB) ray paths and favor a local radial inner core model with ~0.9% velocity perturbation in its top 150 km and small velocity perturbations below. The quality factor in the top 300 km of this inner core region is estimated from *PKP* differential attenuation. Its preferred value is 330 with a lower bound of 75. *INDEX TERMS:* 0935 Exploration Geophysics: Seismic methods (3025); 3260 Mathematical Geophysics: Inverse theory; 7203 Seismology: Body wave propagation; 7207 Seismology: Core and mantle; 8180 Tectonophysics: Tomography; *KEYWORDS:* Earth's core, simulated annealing, network data

Citation: Garcia, R., S. Chevrot, and M. Weber (2004), Nonlinear waveform and delay time analysis of triplicated core phases, *J. Geophys. Res.*, *109*, B01306, doi:10.1029/2003JB002429.

1. Introduction

[2] The arrival times of body waves are the primary source of information exploited in the seismological records. Large data sets have been created [*Engdahl et al.*, 1998] which allowed tomographic studies at both regional and global scales [*Van der Hilst et al.*, 1997; *Bijwaard et al.*, 1998]. The growth of data recorded by seismic networks during the past decade has motivated the search for new methods to routinely measure body wave arrival times. Classically, these methods are based on cross correlations between the different records of a network [*VanDecar and Crosson*, 1990]. Previously, *Chevrot* [2002] described a nonlinear algorithm that permits the estimation of the average waveform recorded by the stations of a seismological network and its time delays at each station. While the analysis of seismograms containing a single prominent seismic phase is relatively simple, seismologists often face complex records when different seismic phases interfere. To demonstrate that the same approach can also be used on such records, we have generalized the algorithm to the case of interfering waves. We focus on the analysis of seismograms in the distance range of the *PKP* triplication. On these kinds of records, interference is particularly strong. We invert for the reference *PKP*(BC) waveform recorded by all the stations, and describe the other body waves as functionals of this reference waveform. This approach therefore incorporates some a priori information in the inversion process.

[3] The paper is organized as follows. Section 2 presents the model parameterization, the a priori information and the simulated annealing algorithm. Section 3 shows examples of applications on triplicated core phases recorded by the Eifel experiment. These examples are chosen in order to demonstrate the potential of the method. The differential travel times and attenuations are analyzed to infer the core structure in section 4. Finally, we discuss the advantages and shortcomings of this approach, and present several possible applications.

2. Method

2.1. A Priori Information and Model Parameterization

[4] The triplication of *PKP*, the *P* phase propagating inside the core, occurs in the epicentral distance range

Copyright 2004 by the American Geophysical Union.
0148-0227/04/2003JB002429$09.00

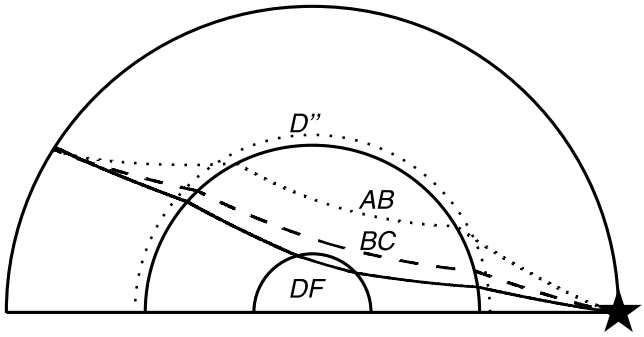


Figure 1. Ray paths of the three *PKP* branches in the Earth: *PKP*(DF) (solid line), *PKP*(BC) (dashed line) and *PKP*(AB) (dotted line). The event (black star) and the D" layer at the base of the mantle are also indicated.

146°–153°. Three core phases interfere: *PKP*(DF) which has its turning point inside the strongly attenuating inner core, *PKP*(BC) which turns at the base of the liquid core, and *PKP*(AB) which turns in the middle of the liquid core, and is proportional to the Hilbert transform of *PKP*(BC) [*Choy and Richards*, 1976; *Creager*, 1992; *Song*, 1997; *Garcia and Souriau*, 2000]. The ray paths of the three core phases are shown on Figure 1. The inner core reflected *PKiKP* phase and the whispering gallery phases (*PKIIKP*, *PK3IKP*...) could be neglected in this epicentral distance range due to their small amplitudes compared to the *PKP* phases. Under this hypothesis, the seismic records of the *PKP* triplication can be modeled as a sum of three seismic phases:

$$\begin{aligned} S_i(t) = {} & R_{DF} G_i^{DF} A(t_i^*) * W(t + \tau_i^{DF}) \\ & + G_i^{BC} W(t + \tau_i^{BC}) \\ & + R_{AB} G_i^{AB} H * W(t + \tau_i^{AB}) \end{aligned} \quad (1)$$

where $S_i(t)$ is the seismogram recorded by station number i; $W(t)$ is the waveform of the *PKP*(BC) phase taken as a reference; $A(t_i^*)$ is a differential attenuation operator; H is the Hilbert transform operator; G_i^{DF}, G_i^{BC}, and G_i^{AB} are the geometrical spreading amplitude corrections computed in the reference Earth's model; R_{DF} and R_{AB} are real parameters standing for relative amplitude corrections; and τ_i^{DF}, τ_i^{BC} and τ_i^{AB} are the time shifts of the *PKP*(DF), *PKP*(BC) and *PKP*(AB) phases, respectively, relative to the beginning of the record. The attenuation operator is defined by $A(t^*) = F[\exp(-\pi f t^*)\exp(2if \ln(f/f_0)t^*)]$, where F is the Fourier transform operator, f is the frequency, and $f_0 = 0.5$ Hz is the reference frequency of *PKP*(DF). This description contains our prior knowledge of the seismic records in the triplication distance range. The model space is thus described by the time samples of the reference waveform $W(t)$, the relative amplitude corrections R_{DF} and R_{AB}, and the different times t_i^*, τ_i^{DF}, τ_i^{BC} and τ_i^{AB} related to each record i.

[5] In the formulation of the problem, we make the implicit assumptions that the source time function is not affected by directivity effects, and that the waveforms are not strongly distorted by mantle heterogeneities. Additionally, we assume that *PKP*(AB) is the Hilbert transform of the *PKP*(BC) phase, and that the *PKP*(DF) phase has the same waveform as the *PKP*(BC) phase, but attenuated. The *PKP*(DF) phase passing through the inner core is more attenuated than the *PKP*(BC) phase which travels only in the outer core where attenuation is low [*Doornbos*, 1983; *Souriau and Roudil*, 1995; *Cormier et al.*, 1998]. Because *PKP*(BC) and *PKP*(DF) phases follow approximately the same ray paths in the crust and the mantle, only short wavelength heterogeneities in the D" layer can distort their relative waveforms [*Bréger et al.*, 1999]. However, *PKP*(AB) and *PKP*(BC) phases follow slightly different ray paths in the mantle, resulting in a larger sensitivity to lateral variations in seismic velocities, particularly in the D" layer [*Bréger et al.*, 2000; *Tkalčić et al.*, 2002]. The network size must not be too large in order to avoid strong waveform variations over the network owing to crustal heterogeneities and directivity effects at the source.

[6] A priori information is also introduced by imposing conditions on the relative time shifts between the different seismic phases. Admissible variations of the differential travel time residuals (BC-DF) and (AB-BC) relative to the reference Earth model AK135 [*Kennett et al.*, 1995] are imposed to lie in the intervals:

$$-2.0 < (\tau_i^{BC} - \tau_i^{DF}) - (t_i^{BC} - t_i^{DF}) < 2.0 \quad (2)$$

$$-2.0 < (\tau_i^{AB} - \tau_i^{BC}) - (t_i^{AB} - t_i^{BC}) < 2.0 \quad (3)$$

where t_i^{DF}, t_i^{BC}, and t_i^{AB} are the theoretical travel times of the three core phases. This a priori information is used to compute the maximum and minimum values of the parameters τ_i^{DF} and τ_i^{AB} at each step of the algorithm. The attenuation parameters t_i^* are allowed to vary between 0.0 and 2.2 s. The parameters R_{DF} and R_{AB} correct for relative amplitude differences between the three *PKP* phases, owing to source radiation and transmission coefficients that produce only smooth amplitude variations within the small epicentral distance range investigated here. No a priori information has been introduced on these two parameters.

2.2. Optimization Algorithm

[7] The inversion is performed by minimizing the following L1 norm misfit (analogous to an energy):

$$E = \sum_i \int |D_i(t) - S_i(t)| dt \quad (4)$$

where $D_i(t)$ and $S_i(t)$ are the observed and synthetic seismograms, and the sums are over the seismograms i and time. The L1 norm is chosen because of its stability with respect to outliers induced by microseismic and high frequency noise, which is critical for a fully nonlinear inversion. The waveform inversion is performed following a simulated annealing (SA) algorithm close to the algorithm described by *Chevrot* [2002]. SA optimization algorithms have been widely applied in geophysics [*Sen and Stoffa*, 1995; *Sharma and Kaikkonen*, 1998] and more recently to teleseismic data [*Kolář*, 2000; *Chevrot*, 2002]. The simulated annealing algorithm is a Monte Carlo Markov Chain algorithm with the probability of uphill investigation of the misfit function decreasing along the cooling schedule. The reader is referred to the references cited above for a full description of the simulated annealing algorithm. The simulated annealing algorithm is optimal for the inversion

of the waveform $W(t)$ [*Kuperman et al.*, 1990; *Chevrot*, 2002] because energy computations are restricted to the computation of energy differences at each time step of the waveform $W(t)$.

[8] The algorithm used in our study is a variation of the very fast simulated annealing (VFSA) [*Sen and Stoffa*, 1995]. An exponential cooling schedule [*Salamon and Berry*, 1983; *Nulton and Salamon*, 1988; *Andresen and Gordon*, 1994] of the form $T(k) = \gamma^k T(0)$ is implemented with $\gamma = 0.98$ and $N = 1500$ iterations. The starting temperature $T(0)$ is fixed at three times the value of the initial misfit in order to start well above the critical temperature of the system, and $T(1500) \approx 10^{-14} T(0)$. At each temperature step, 5 random perturbations are implemented for each parameter P_j, and selection is done according to Boltzmann statistics. Each perturbation consists in perturbing the waveform parameters $W(t)$ and the amplitude parameters R_{DF} and R_{AB} by $\pm\Delta W$, with $|\Delta W| = 0.01|W|_{\max}$, following the scheme described by *Chevrot* [2002]. The other model parameters P_j are randomly perturbed at each step l according to the rule

$$P_j^{l+1} = P_j^l + y_j(P_j^{\max} - P_j^{\min}) = P_j^l + y_j \Delta P_j \tag{5}$$

where the random number y_j follows a Cauchy distribution parameterized by temperature T_j [*Sen and Stoffa*, 1995]:

$$y_j = \operatorname{sign}\left(u_j - \frac{1}{2}\right) T_j \left[\left(1 + \frac{1}{T_j}\right)^{|2u_j - 1|} - 1\right] \tag{6}$$

where u_j is a real number selected randomly in the interval [0, 1]. The main difference to the VFSA algorithm is that the temperature T_j is related to the energy $E(k)$ and not to the temperature $T(k)$ of the system. The temperature describing the Cauchy probability of y_j is defined by

$$T_j = \left(\frac{E(k)}{E(0)}\right)^2 \tag{7}$$

where $E(k)$ is the energy of the system. As the energy of the system decreases, the temperature T_j decreases and reduces the area explored in the parameter space. This procedure is chosen in order to adapt the random variations of the parameters to the convergence level of the system, and not to an arbitrary cooling schedule.

[9] In order to solve cycle skipping ambiguity on noisy traces, an additional modification of the SA algorithm is introduced. Once the system has reached a good convergence level, the parameters τ_i^{DF}, τ_i^{BC} and τ_i^{AB} are reinitialized to the median value of their residuals relative to the *PKP*(BC) phase at all the stations, and admissible variations of the differential travel time residuals are limited to ±1 s. This procedure introduces additional a priori information on the time shifts, which allows to obtain coherent results even for noisy records.

[10] The a posteriori covariance matrix is estimated following a method described by *Sharma and Kaikkonen* [1998]. Twenty runs of the SA algorithm are performed with different random number seeds, and the covariance matrix is estimated from the results obtained for the twenty inversions. This statistical method allows to compute errors even for model parameters for which error bars are difficult to estimate, such as the t_i^* parameters. An average model is also computed, and the model presenting the lowest energy over the twenty runs is kept as the best model.

[11] The running time of the SA algorithm depends on the number of seismograms, the time window length, and the sampling rate. For 150 seismograms, sampled at 20 Hz, with a time window of 35 s, the SA algorithm runs in 100 CPU minutes on a linux PC Pentium IV at 1.7 GHz. However, the CPU running time could be divided by a factor of 5 by increasing the cooling speed of the algorithm. In this case, the differential travel times are properly resolved, but the differential attenuations are unstable.

[12] The power of the nonlinear waveform inversion with SA is illustrated in section 3 with a few examples taken from the Eifel experiment [*Ritter et al.*, 2000]. These examples are chosen to demonstrate the ability of the method to investigate interfering *PKP* branches as well as their interference with depth phases.

3. Examples

[13] To illustrate the potential of the method, we present three examples showing increasing degrees of complexity. The data set consists of core phases recorded by the temporary Eifel experiment in the 146°–153° epicentral distance range, and includes waveforms from about 150 broadband and short period stations installed in central Europe in the Eifel plume region [*Ritter et al.*, 2000]. This dense temporary network covered an area of 3° by 3° (Figure 2). the instrument responses are deconvolved from the data, which are filtered by a band-pass butterworth filter with corner frequencies at 0.3 Hz and 1.5 Hz. The data set is composed of the records of eight earthquakes that occurred in the Fiji-Tonga subduction zone (Table 1), three of which are presented in details in the next sections.

3.1. A Simple Case: Three Core Phases That Are Well Separated in Time

[14] The 152 stations of the Eifel network have recorded the three core phases generated by earthquake 8 (Table 1). The data, filtered between 0.3 and 1.5 Hz and aligned on the theoretical arrival time of the *PKP*(BC), are presented on Figure 3a. The three *PKP* phases are clearly separated in this distance range, and the noise level is low. The *PKP*(DF) phase is characterized by a lower frequency content and a smaller amplitude than the *PKP*(BC) phase owing to inner core attenuation [*Souriau and Roudil*, 1995; *Cormier et al.*, 1998]. Figure 3b shows the comparison between data and the synthetic waveforms for the best model once all the seismograms are aligned on the *PKP*(BC) arrival time. The fit is very good for *PKP*(DF) and *PKP*(BC) phases, and quite good for the *PKP*(AB) phase. The energy and variance reductions for the whole data set are 34% and 52%, respectively. The unexplained energy and variance reflects the noise level and the parts of the seismograms that are not fitted by the *PKP* synthetic phases. Figure 3c presents the differential time shifts $\tau_i^{DF} - \tau_i^{BC}$ and $\tau_i^{AB} - \tau_i^{BC}$. The small amount of scattering of the measurements is indicative of their accuracy. Measurement error bars are generally lower than 0.5, 0.2, and 0.4 s for *PKP*(DF), *PKP*(BC), and *PKP*(AB) phases, respectively.

[15] Figure 4 presents a comparison between the RMS error estimated by a statistical analysis of the 20 inversion

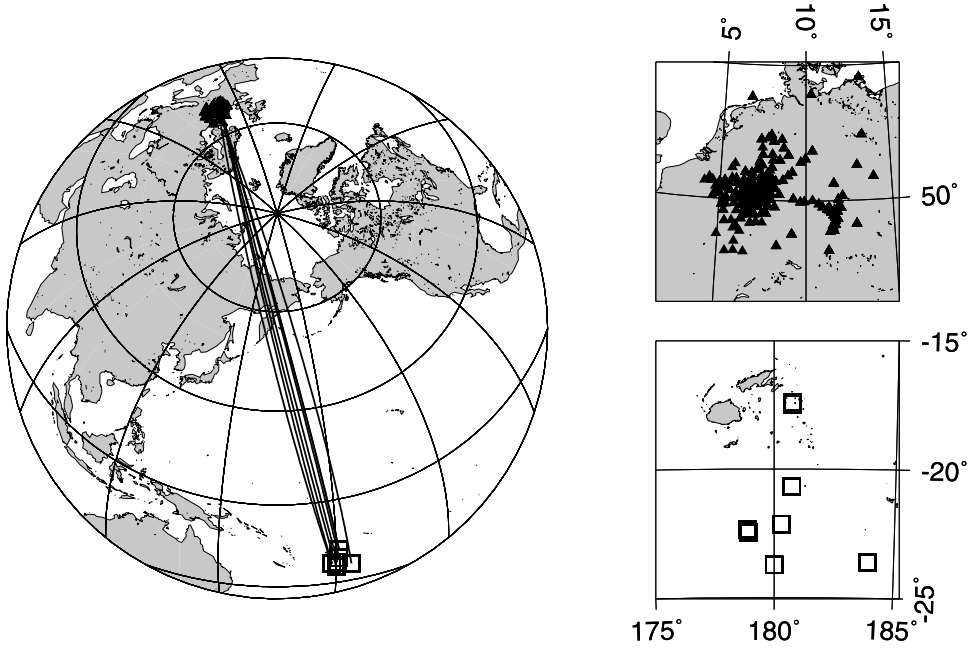


Figure 2. On the left, stations (solid triangles) and events (open squares) locations with typical great circle paths (solid lines). On the right, zoom of the (top) receiver and (bottom) source regions.

results, and the error computed from the waveforms given by the best model using a cross-correlation method [*Chevrot*, 2002]. The error estimated by cross correlation is always smaller than 0.5 s. The statistical study of the models after inversion separates the records in two groups. The records properly fitted present time shifts with a very low statistical error, indicating that the 20 inversions give the same results for these parameters. On the other hand, a small number of noisy records present time shifts with statistical errors larger than the errors estimated by cross correlation owing to cycle skipping ambiguity, which generates multiple local minima in the misfit function, and so different results are obtained for the same parameter over the 20 inversions. Therefore the statistical error estimate gives information on the shape of the misfit function and on the cycle skipping ambiguity that is not accessible through the cross-correlation method.

[16] Figure 5 presents typical evolutions of the different parameters during the cooling schedule for the 20 inversions performed. The energy shows a strong decrease close to the temperature step $k = 750$, corresponding to the critical temperature, and is approximately flat from steps 800 to 1500. At this stage, the time shifts are artificially modified in order to overcome possible cycle skipping problems, as described above. This perturbation introduces a step like energy increase, from which the system quickly recovers. Amplitude correction parameters R_{DF} and R_{AB} are converging once the critical temperature is attained, but the final values for R_{DF} are scattered owing to a trade-off between R_{DF} and attenuation parameters t_i^*. In this example, $R_{DF} = 1.34 \pm 0.04$ and $R_{AB} = 0.39 \pm 0.004$, and the standard deviations of these parameters are lower than 0.06 for all the other earthquakes analyzed in this study. The other plots show the evolution of the inverted parameters for a randomly chosen seismogram. These parameters present large variations before the critical temperature, beyond which they quickly converge to their final value. This value is slightly perturbed by the procedure at step $k = 750$, but convergence is achieved at the end of the algorithm. The convergence time is the longest for the t_i^* parameter, because a preliminary alignment of the *PKP*(DF) waveform is necessary, which simply results from the fact that energy variations due to t_i^* are small compared to the ones related to the other parameters. The set of final values for t^* generally shows the largest scatter, which indicates that it is the most poorly resolved. The different runs show that t^* converges to different values suggesting the existence of local minima for the misfit function.

3.2. Interference of the Three Core Phases

[17] The method has been tested in the case of interfering core phases with synthetic data computed with the WKBJ software [*Chapman*, 1978] including attenuation in the inner core and additional small amplitude core phases (*PKiKP*, *PKIIKP*...). As seen on Figure 6a, the inner core reflected *PKiKP* phase has a small effect on the data fit just after the *PKP*(BC) phase for epicentral distances in between 147 and 148°. However, it does not change significantly the retrieved reference waveform and output parameters because *PKiKP*

Table 1. Characteristics of the Events Used in This Study, Extracted From the Preliminary Determination of Epicenter

Event	Date	Time, UT	Latitude, deg	Longitude, deg	Depth, km	M_w
1	27 Jan. 1998	0214:13.0	−20.68	−179.27	646.0	5.3
2	27 Jan. 1998	1955:00.0	−22.46	178.93	608.8	5.4
3	27 Jan. 1998	2105:44.0	−22.34	178.90	610.0	5.5
4	29 March 1998	1948:16.0	−17.42	−179.24	539.0	6.4
5	29 March 1998	2038:40.0	−17.49	−179.26	526.7	5.4
6	11 April 1998	0044:35.0	−23.60	−176.08	33.0	4.3
7	14 April 1998	0341:21.0	−23.73	−180.00	494.4	5.3
8	16 May 1998	0222:03.0	−22.14	−179.70	586.0	5.9

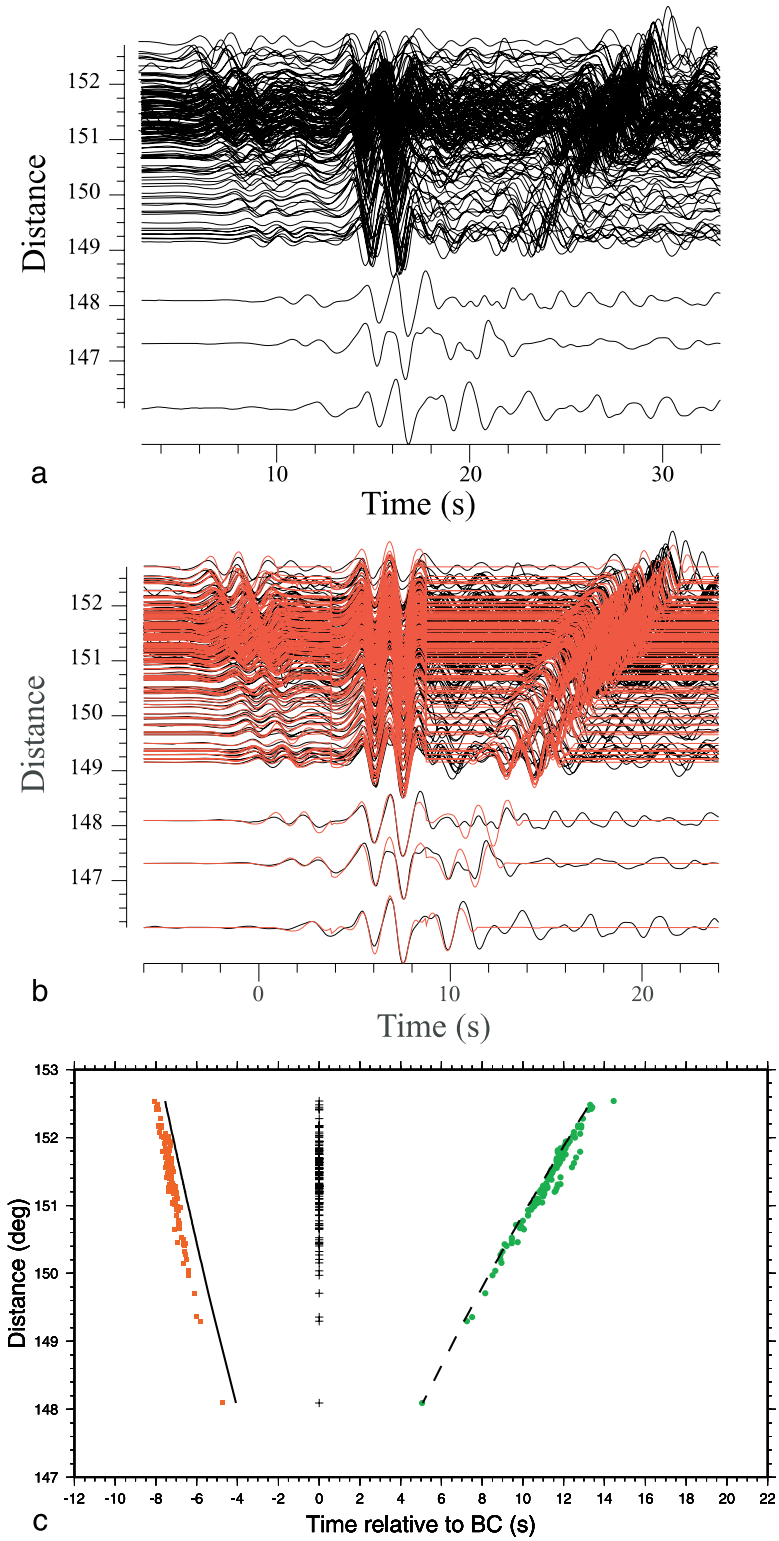


Figure 3. Example 1. (a) Raw data before inversion, aligned on the theoretical arrival time of *PKP*(BC) and plotted as a function of their epicentral distance (in degrees). (b) Data (black lines) and best model synthetic seismograms (red lines) aligned on the *PKP*(BC) phase. (c) Best model arrival times of the three *PKP* phases relative to *PKP*(BC). Dashed lines indicate theoretical arrival times predicted by the ak135 reference Earth's model.

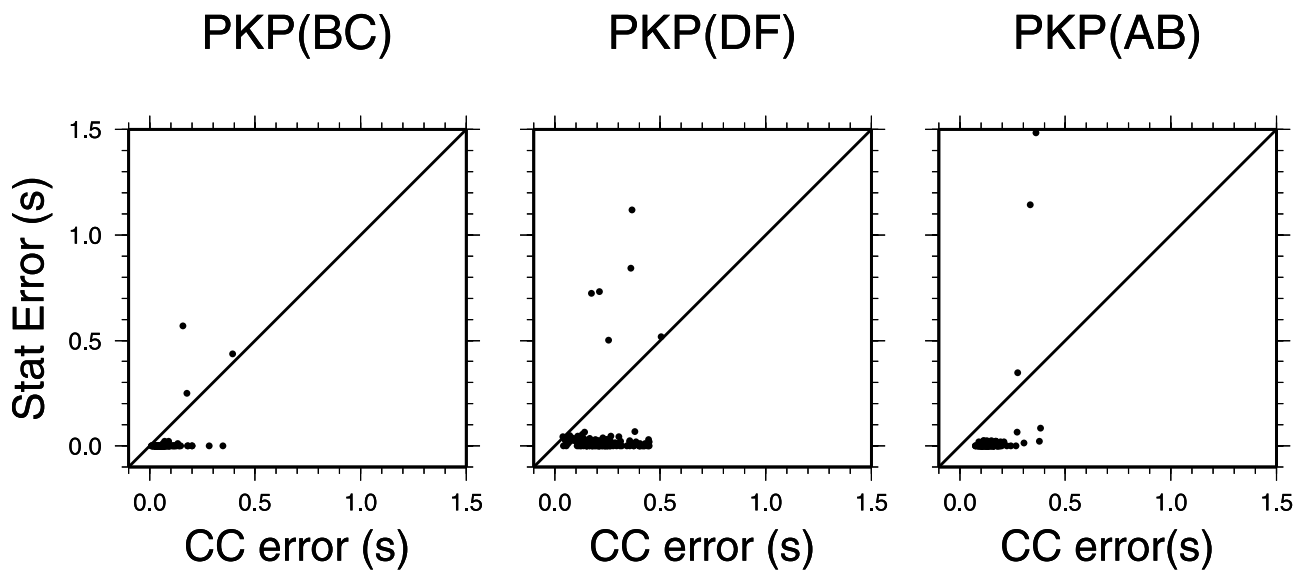


Figure 4. Statistical estimate of the time shifts RMS errors (in seconds) plotted as a function of the error computed for the best model using the cross correlation method described by *Chevrot* [2002]. From left to right, errors of the parameters τ_i^{BC}, τ_i^{DF}, and τ_i^{AB}. The line indicates the one to one correspondence.

and *PKP*(BC) phases have different ray parameters, so that the two phases are easily separated by the network. This synthetic test demonstrates that the waveforms are properly fitted, the travel time residuals properly recovered, and the inner core reflected *PKiKP* phase has only a small effect on the results.

[18] 123 stations of the Eifel network have recorded core phases generated by earthquake 4 (see Figure 7). The records have been processed as for Figure 3. In this distance range (146°–149°), the three *PKP* phases arrive within 4 to 8 s of each other. Since the waveform is about 5 s long, the three core phases strongly interfere. The data fit and the time shift parameters are presented in Figures 7b and 7c, respectively. The energy and variance reduction of the whole data set are 59% and 80%, respectively. These results show that the nonlinear inversion is able to retrieve the model parameters even when the three phases strongly interfere.

3.3. Complex Source Time Functions and Presence of Depth Phases

[19] The method has been tested in the case of a complex source time function by including depth phases in the computation of synthetic data for an earthquake at 35 km depth. In this case, the direct *PKP* phases interfere with the depth phases, perturbing the waveforms and making the pick of individual phases difficult. The nonlinear inverse problem is solved with a reference waveform of 18 s length in order to include the depth phase *pPKP*(BC). The results are presented on Figure 8. They demonstrate that the waveforms and differential travel times are properly recovered, and that the output waveforms include both direct *PKP* and the corresponding depth phase.

[20] For event 6, only the 27 stations corresponding to epicentral distances smaller than 153° are selected, because the *PKP*(BC) phase is strongly diffracted at larger epicentral distances. The data fit and the time shift parameters are shown on Figures 9a and 9b, respectively. Despite the presence of depth phases, the data fit is comparable to the previous examples (39% energy reduction and 58% variance reduction), and the time shifts fit quite well those predicted by the reference Earth model. The reason is that the window length is chosen large enough to include both *PKP* and *pPKP* phases for each core phase. The inverted waveforms of the three core phases are presented on Figure 9c. They exhibit two energy arrivals, the first one corresponding to the direct phase and the second one to the depth phase. The differential time between the two phases is about 11 s (corresponding to a hypocentral depth of 33 km when computed in the CRUST5.1 model [*Mooney et al.*, 1998]) which is in excellent agreement with the results of the preliminary determination of epicenters. This example demonstrates that model parameters can be retrieved even for long (16 s in this case) and complex source time functions allowing the measurement of the differential travel times for large magnitude earthquakes. Moreover, the algorithm is also successful for a small number of records. Some tests performed on high-quality data have even shown that the method can work for a single record with clearly separated phases.

4. Interpretation of the Results

[21] In section 3, three examples of core phase data analysis have been presented in detail. The entire Eifel core phase data set, not shown here, has been analyzed following the method described in section 2. We will now report the interpretation of differential travel times and attenuations in terms of Earth structure. The use of differential travel times allows us to significantly reduce the errors related to event mislocations. In addition, 1 Hz *PKP*(DF) and *PKP*(BC) Fresnel zones overlap in the crust and the mantle, reducing the contribution of heterogeneous structures in these parts of the Earth. However, because the sources are close to each others, each core phase samples the same region of the Earth, and the tomographic problem is ill-posed. For this

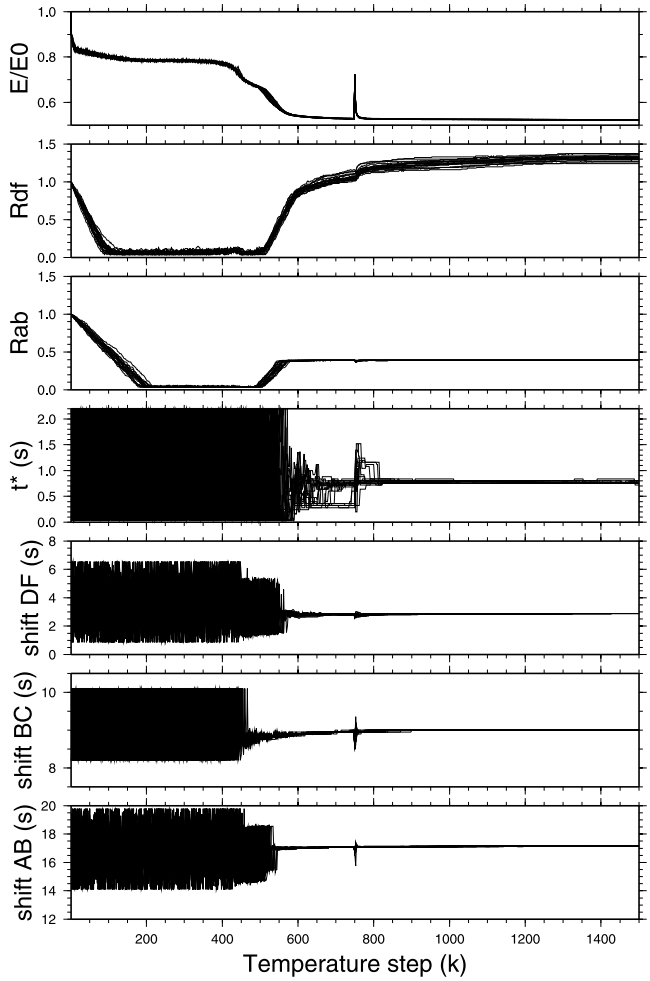


Figure 5. Energy, R_{DF}, R_{AB} and parameters of a randomly selected seismogram for the 20 SA inversions, as a function of the temperature step (k) describing the cooling schedule. From top to bottom: energy normalized to its starting value [$E(k)/E(0)$], R_{DF}, R_{AB}, parameter t_1^* in seconds, and parameters τ_1^{DF}, τ_1^{BC}, and τ_1^{AB} in seconds.

reason, we will not perform a direct inversion of these measurements to retrieve the average Earth structure along these paths.

4.1. AB-BC Differential Travel Times

[22] The two core phases *PKP*(BC) and *PKP*(AB) follow significantly different ray paths in the Earth, with takeoff angles and hit points of the rays at the core-mantle boundary (CMB) separated by more than 10°. As a result, the AB-BC differential travel time residuals can be influenced by the Earth structure at the source or at the receiver [*Helffrich and Sacks*, 1994], or, owing to *PKP*(AB) grazing incidence at the CMB, by lower mantle heterogeneities [*Bréger et al.*, 2000; *Tkalčić et al.*, 2002]. Figure 10 presents differential travel times obtained for three earthquakes very close to each others in the Fiji Islands region. The differential travel time plots show similar features. The *PKP*(DF) phase arrives earlier than predicted by the ak135 Earth's model [*Kennett et al.*, 1995], and its advance increases as the epicentral distance decreases. The *PKP*(AB) phase presents anomalously late arrivals, that are shown in red on the plots. These positive AB-BC differential travel time residuals can be associated with anomalous structure along the *PKP*(AB) ray path, because such large anomalies are not seen on the BC-DF differential travel times. When plotted at *PKP*(AB) entry and exit points at the core-mantle boundary, the differential travel time residuals shows a clear azimuthal variation. Figure 11 separates anomalous from normal data and demonstrates that this feature is not due to cycle skipping problems. However, as seen on Figure 10, the recent tomographic models of the lowermost mantle [*Bijwaard et al.*, 1998; *Kárason and Van der Hilst*, 2001] do not present sharp lateral velocity contrasts which are able to explain the *PKP*(AB) travel time anomalies. Similar anomalous *PKP*(AB) travel times have already been observed in the same region [*Luo et al.*, 2001] and interpreted in terms of sharp lateral velocity gradients at the core-mantle boundary. Unfortunately, it is not possible with the present data set to specify the location, along the *PKP*(AB) ray paths, of the Earth structure at the origin of these travel time anomalies. Despite their poor resolution, these results show the presence of large amplitude short wavelength heterogeneities, and demonstrate the ability of the method to recover small-scale information from the records of large seismic networks.

4.2. BC-DF Differential Travel Times and Attenuations

[23] The two core phases *PKP*(BC) and *PKP*(DF) follow very close ray paths in the crust and the mantle, with takeoff angle differences smaller than 5°. These two core phases sample the same heterogeneities in the crust and the mantle, a property that has been widely used in BC-DF differential travel time residual studies [*Tanaka and Hamaguchi*, 1997; *Isse and Nakanishi*, 2002]. The BC-DF differential travel time residuals obtained for the whole Eifel core phase data are presented in Figure 12 as a function of epicentral distance and bottom radius of the *PKP*(DF) rays. A general trend is seen: the smaller the epicentral distance the larger the BC-DF residuals. The BC-DF differential ray parameters show large deviations from the differential ray parameter predicted by the ak135 Earth's model. The residual of BC-DF differential ray parameter ranges form −0.5 s/° at 147° epicentral distance to −0.2 s/° for epicentral distances larger than 150°. A least squares inversion of BC-DF differential travel time residuals has been performed for a simple radial inner core model composed of four homogeneous layers: one layer of 150 km thickness at the top of the inner core and three layers of 50 km thickness below. Inner core lateral velocity perturbations are excluded because the array data analysis do not show any back azimuth deviation of the *PKP*(DF) phase compared to *PKP*(BC). The resulting model is plotted with error bars at the bottom of Figure 12, and the data fit is shown by thick grey lines in the two plots at the top. With 65% variance reduction, the inner core model reproduces quite well the trends seen on the data. The velocity perturbation in the inner core is averaged in the top 150 km because none of the *PKP*(DF) rays have their turning point in this layer. However, the inferred ∼0.9% velocity perturbation agrees quite well with recent studies [*Niu and Wen*, 2001; *Garcia*, 2002; *Isse and Nakanishi*, 2002]. Below 150 km depth in the inner core,

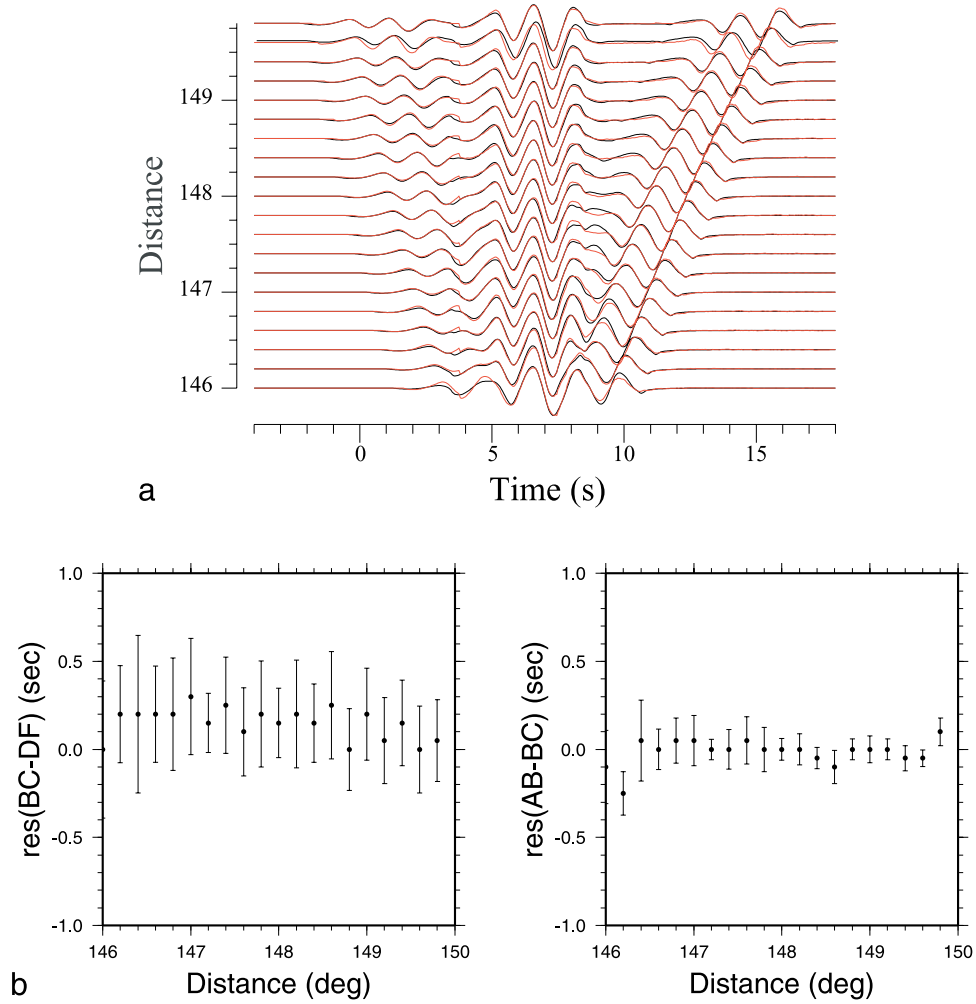


Figure 6. Nonlinear analysis of synthetic *PKP* data computed with the WKBJ software for an earthquake at 610 km depth. (a) WKBJ synthetic seismograms (black lines) and synthetic seismograms predicted by the best model (red lines) aligned on the *PKP*(BC) phase. (b) BC-DF and AB-DF best model residuals as a function of epicentral distance.

a better resolution is achieved, and smaller velocity perturbations are obtained. A comparison with IASP91 [*Kennett and Engdahl*, 1991] and PREM [*Dziewonski and Anderson*, 1981] inner core seismic models is also provided on Figure 12c. The poor spatial sampling of the inner core by the data has two important consequences. First, the inner core model is local, and it should not be interpreted as an average inner core model. Second, the inner core anisotropy can not be resolved because the data sample a short range of ξ angles between the tangent of the ray in the inner core and the spin axis of the Earth ($50° < \xi < 57°$).

[24] As seen in section 3, the t^* parameter describing the differential attenuation between *PKP*(BC) and *PKP*(DF) is the worst resolved parameter. For this reason, t_i^* parameters with statistical errors larger than 0.1 s are excluded from the analysis. Figure 13 presents the t_i^* parameters obtained for the whole Eifel core phase data. For epicentral distance larger than about 152°, the differential attenuation decreases strongly, because the amplitude of the *PKP*(BC) phase is reduced by diffraction at the inner core boundary [*Souriau and Poupinet*, 1991]. The distribution of the inner core attenuation parameter suggests that t^* is less than 1.5 s for epicentral distances lower than 153°. The corresponding attenuations are presented through the parameter 10,000/Q as a function of *PKP*(DF) turning point depth below the inner core boundary, following *Helffrich et al.* [2002]. This plot puts an upper bound of ~130 on the $10{,}000/Q$ parameter, corresponding to a lower bound of ~75 on the inner core quality factor in this region. The average value of the inner core quality factor in its top 300 km is ~330. This value favors low attenuation models [*Doornbos*, 1974; *Souriau and Romanowicz*, 1996] for the same region in the inner core, even if the lower bound does not exclude high attenuation models [*Niazi and Johnson*, 1992; *Bhattacharyya et al.*, 1993; *Helffrich et al.*, 2002].

5. Discussion

5.1. Advantages and Limitations of the Method

[25] The method of nonlinear waveform inversion and differential travel time estimates presents numerous advantages:

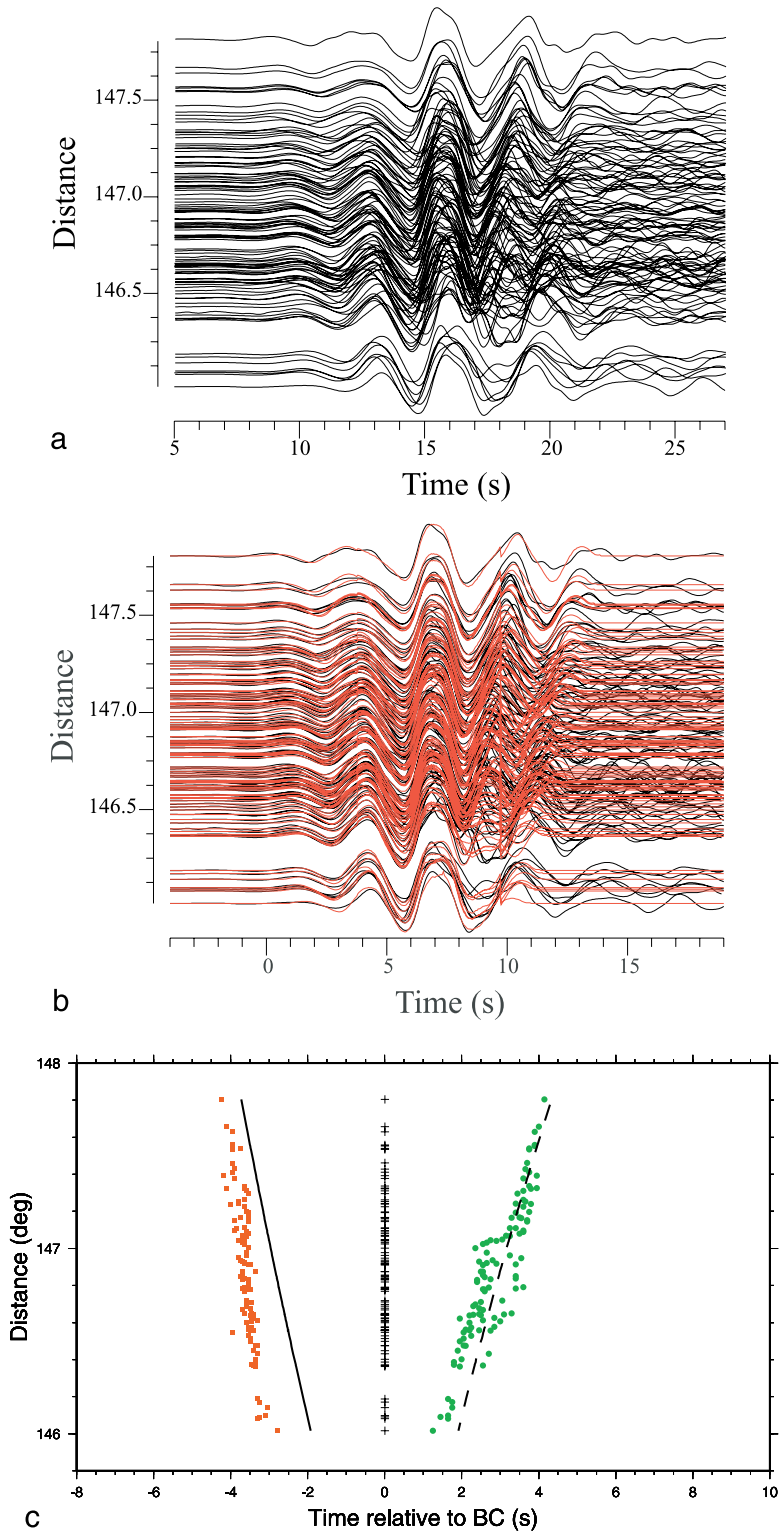


Figure 7. Example 2. (a) Raw data before inversion, aligned on the theoretical arrival time of *PKP*(BC), and plotted as a function of their epicentral distance (in degrees). (b) Data (black lines) and best model synthetic seismograms (red lines) aligned on the *PKP*(BC) phase. (c) Best model arrival times of the three *PKP* phases relative to *PKP*(BC). Dashed lines indicate theoretical arrival times predicted by the ak135 reference Earth's model.

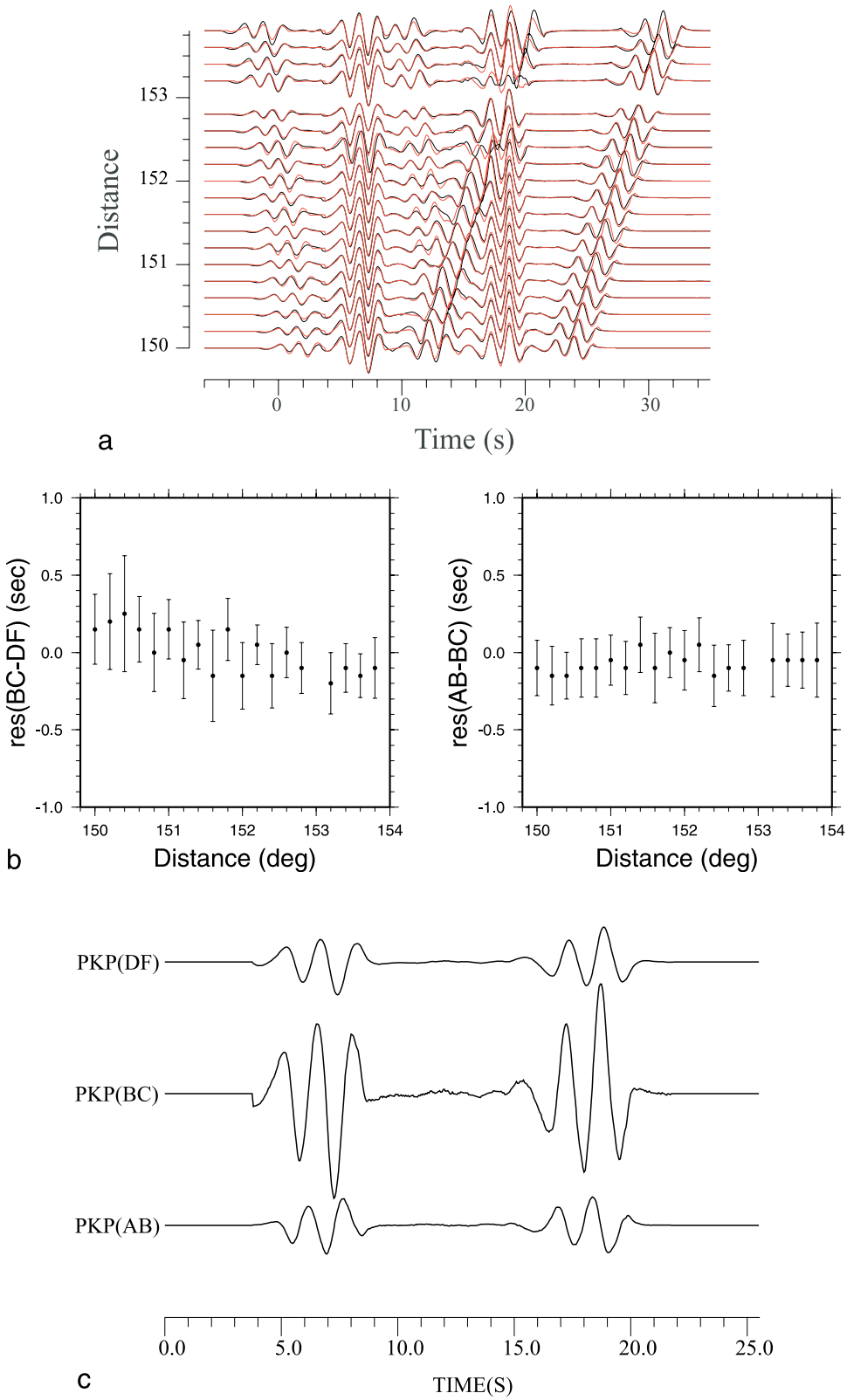


Figure 8. Nonlinear analysis of synthetic *PKP* data computed with the WKBJ software for an earthquake at 35 km depth. (a) WKBJ synthetic seismograms (black lines) and best model synthetic seismograms (red lines) aligned on the *PKP*(BC) phase. (b) BC-DF and AB-DF best model residuals as a function of epicentral distance. (c) From top to bottom, output *PKP*(DF), *PKP*(BC), and *PKP*(AB) waveforms including both the direct *PKP* phase and the corresponding *pPKP* depth phase.

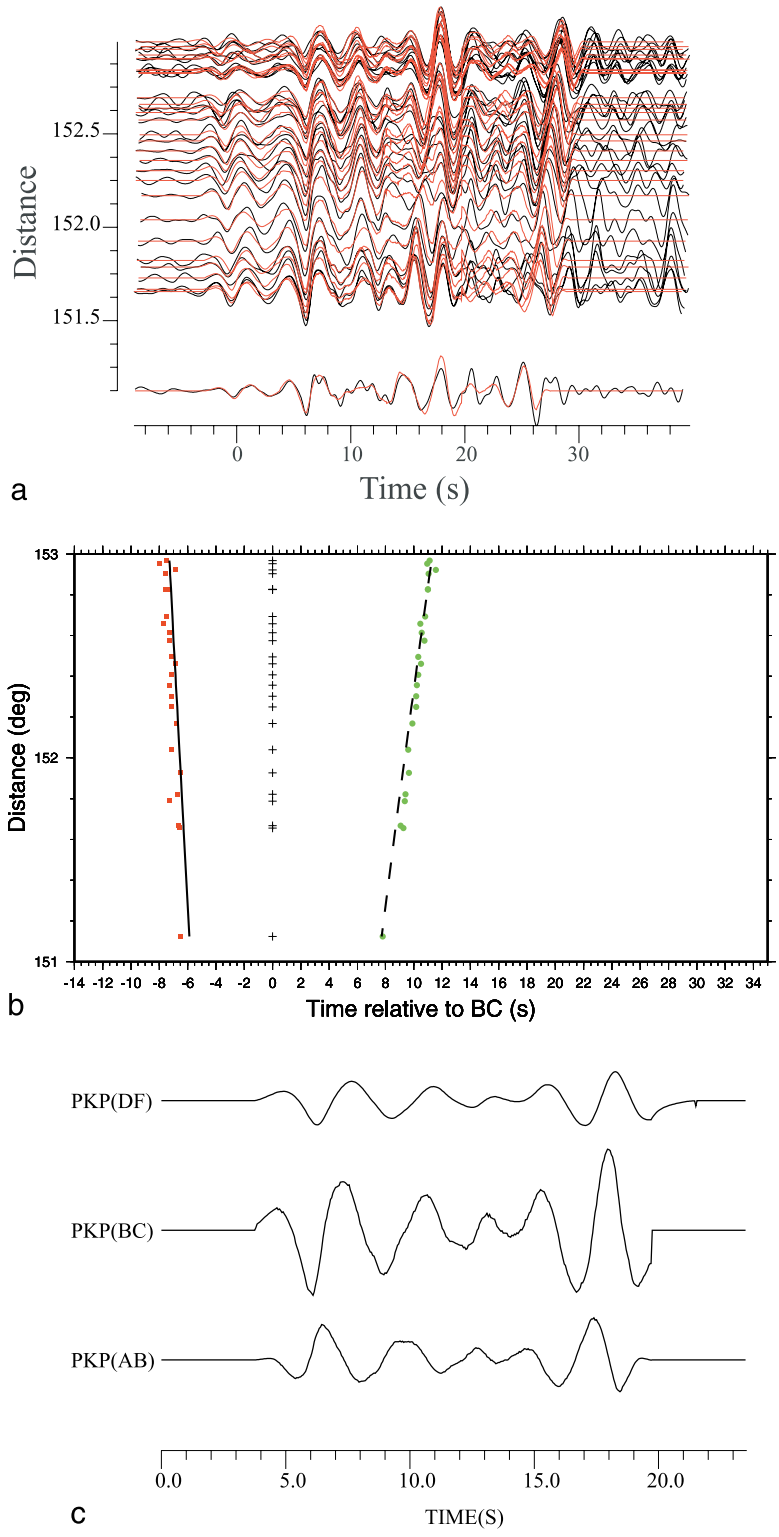


Figure 9. Example 3. (a) Data (black lines) and best model synthetic seismograms (red lines) aligned on the *PKP*(BC) phase. (b) Best model arrival times of the three *PKP* phases relative to *PKP*(BC). Dashed lines indicate theoretical arrival times predicted by the ak135 reference Earth's model. (c) From top to bottom, waveforms obtained after inversions for *PKP*(DF), *PKP*(BC), and *PKP*(AB) phases as a function of time (s). Notice the two energy arrivals associated to direct and depth phases.

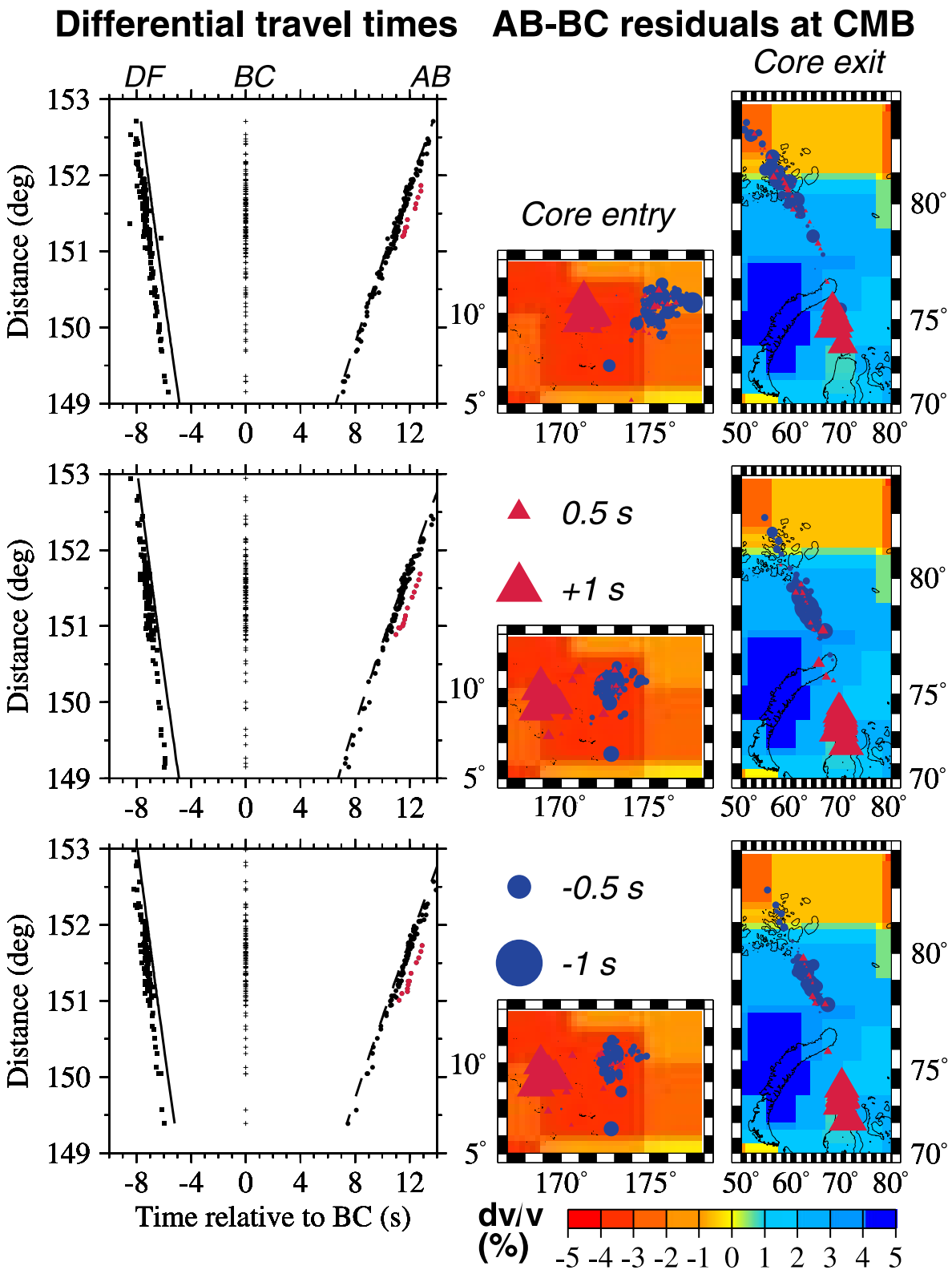


Figure 10. Interpretation of AB-BC differential travel time residuals. On the left, from top to bottom, differential travel times for events 2, 3, and 8 on Table 1. For each earthquake, the arrival times of the three core phases relative to *PKP*(BC) are plotted as a function of epicentral distance. The anomalous positive AB-BC residuals are shown in red, and the theoretical arrival times predicted by the ak135 Earth model are shown as solid and dashed lines. On the right, zero mean AB-BC differential travel time residuals are plotted at the entry and exit points in the core of the *PKP*(AB) rays, superimposed on the *Bijwaard et al.* [1998] *P* velocity model of the lowermost mantle. Positive AB-BC differential travel time residuals are shown with red triangles and negative residuals are shown with blue circles.

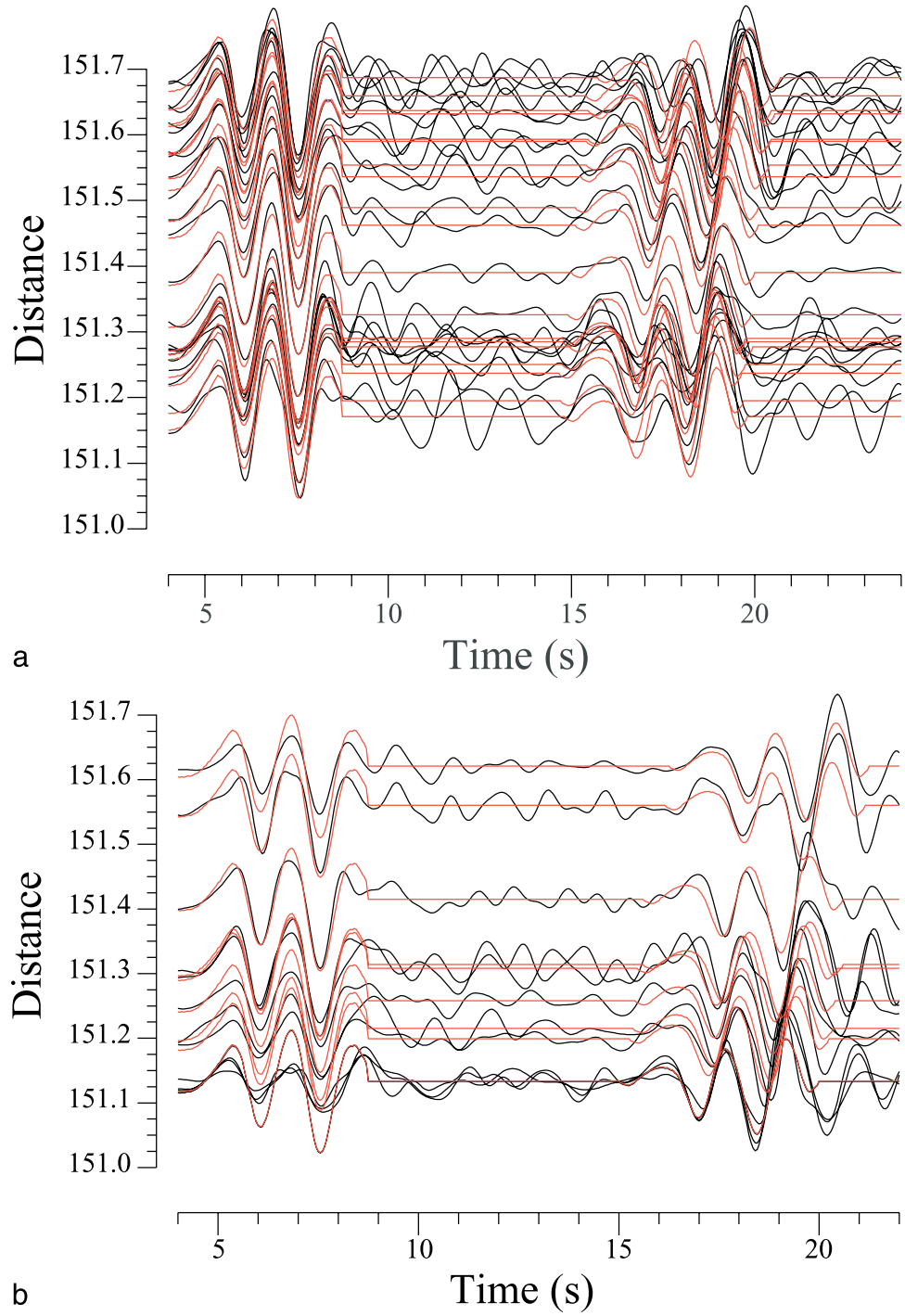


Figure 11. Closeup on the records of event 8 presenting (a) nominal *PKP*(AB) arrivals on top and (b) late arrivals on the bottom. Data (black lines) and synthetics (red lines) are aligned on the *PKP*(BC) phase seen on the left of the record sections. The *PKP*(AB) phase is properly fitted on both plots demonstrating that the larger AB-BC residuals are not due to cycle skipping problems. A similar pattern is observed for the AB-BC anomalous residuals of events 2 and 3.

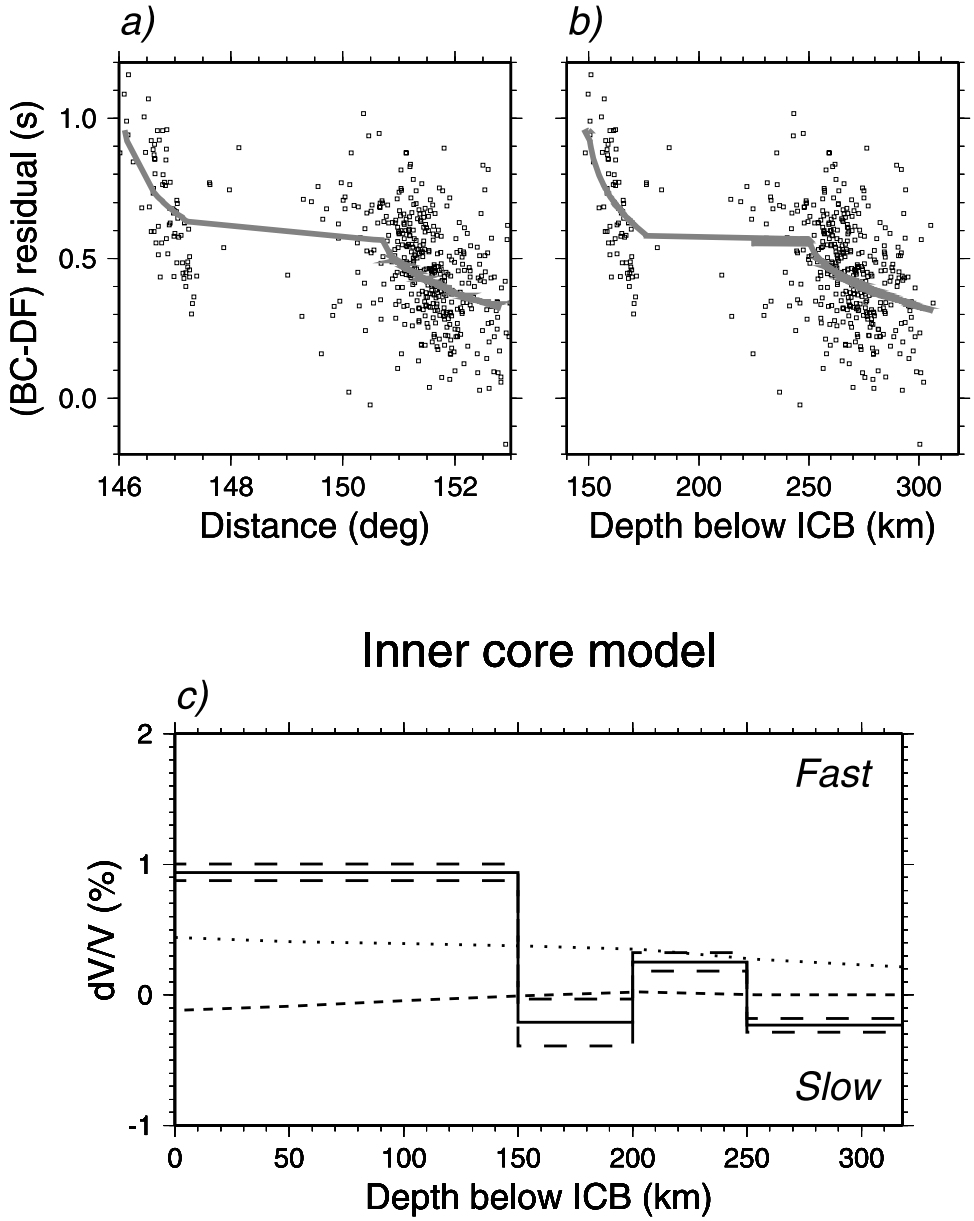


Figure 12. BC-DF differential travel time residuals for the ak135 Earth model and corresponding inner core model. (a) BC-DF differential travel time residuals are plotted as a function of epicentral distance and (b) maximum depth of the *PKP*(DF) rays in the inner core. Thick grey lines indicate BC-DF residuals predicted by the radial inner core model. (c) Velocity perturbation (%) as a function of depth in the inner core, obtained after inversion of the differential travel times residuals for an inner core model composed of four homogeneous layers. Solid and long dashed lines indicate the average and the standard deviation of the inner core velocity perturbation model, respectively. IASP91 (dotted line [*Kennett and Engdahl*, 1991]) and PREM (short dashed line [*Dziewonski and Anderson*, 1981]) inner core models are presented for comparison.

[26] 1. The method is simple and can be used routinely and automatically, since only the length of the reference waveform must be selected.

[27] 2. The search for a global minimum is successful even on noisy data.

[28] 3. The nonlinear inversion algorithm allows to estimate waveforms and differential travel times even when the three phases interfere on the seismograms. This is also valid for shallow earthquakes in which depth phases (*pPKP*) interfere with direct phases (*PKP*).

[29] 4. The waveform $W(t)$ can be used to estimate the source time function of the event [*Kolář*, 2000]. Moreover, if $W(t)$ includes both direct and depth phases (*PKP* + *pPKP*), it can be used to estimate the event depth and the structure of the crust at the source.

[30] 5. The method can be extended to the more general problem of estimating multiple teleseismic arrivals with an equation of the form $S_i(t) = W(t) * G_i(t)$, where $W(t)$ stands for a reference phase representing a crude estimate of the source time function of the event, and $G_i(t)$ is a model

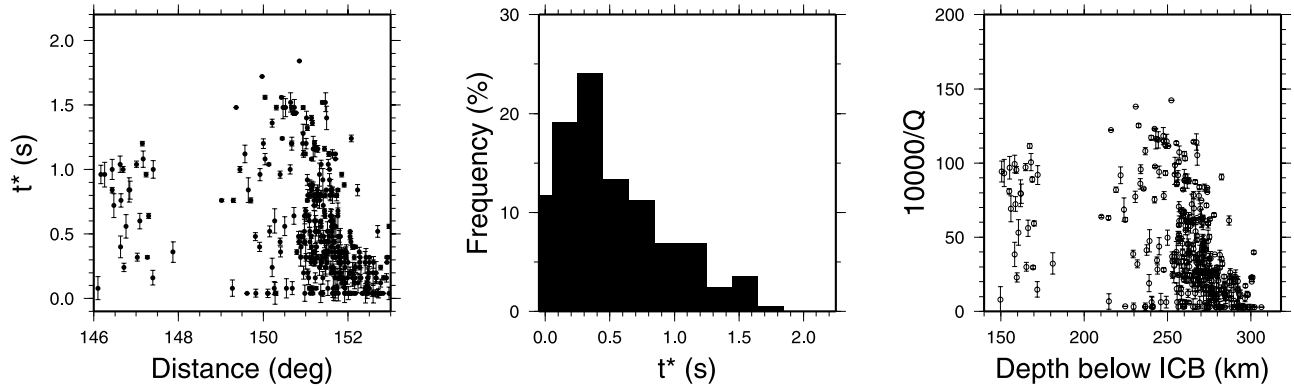


Figure 13. (left) BC-DF differential attenuation parameters t^* (s) as a function of epicentral distance (°). (middle) Histogram of BC-DF differential attenuation parameters t^*. (right) Inner core attenuation parameter $q = 10{,}000/Q$ is shown as a function of depth of the *PKP*(DF) turning point in the inner core (km). Over the whole Eifel core phase data set, only t^* parameters presenting statistical errors lower than 0.1 s are plotted.

response describing the propagation of the different teleseismic phases present in the seismograms. In our case, using the geometrical optics framework:

$$G_i(t) = R_{DF} G_i^{DF} A(t_i^*) * \delta(t + \tau_i^{DF}) + G_i^{BC} \delta(t + \tau_i^{BC}) + R_{AB} G_i^{AB} H * \delta(t + \tau_i^{AB}).$$

Nevertheless, some limitations come from the approximations used. A first limitation is related to the source excitation. Because the source radiation must be similar for the rays arriving at the different stations, takeoff angles must not be too close to a nodal plane. A second limitation is related to the body wave paths in the Earth: waveform distortions produced by scattering have to be small, and the near receiver crustal reverberations must be the same for the different stations.

5.2. Conclusion

[31] The parameterized inversion described in this study has proven to be very efficient in estimating relative arrival times and attenuations of seismic body waves, even when they interfere or when depth phases are present in the records. This method allows to analyze the *PKP* triplication in an epicentral distance range previously unexplored due to the complexity of the records. This approach opens new possibilities to study the fine structure of the inner core, the D" layer and the mantle discontinuities through the investigation of *PKP* and *P* triplications. Moreover, the method can be extended to more complex parameterizations, including an estimate of the source time function and focal mechanism.

[32] AB-BC differential travel time residuals indicate the presence of large-amplitude and small-scale heterogeneities along the *PKP*(AB) ray paths. The interpretation of BC-DF differential travel time residuals in terms of radial inner core structure leads to a local inner core model with ~0.9% velocity perturbation in the top 150 km of the inner core and small velocity perturbations below. The BC-DF differential attenuations put a lower bound of 75 and an average of 330 on the quality factor in the top 300 km of the inner core for this region, and for frequencies between 0.3 and 1.5 Hz.

[33] **Acknowledgments.** We acknowledge two anonymous referees and JGR Associate Editor for their help in improving the manuscript. We thank Martin Budweg and the Eifel plume team for acquiring the data, for providing us the core phase data, and for their technical support on this data set. Seismic instruments for the experiment were supplied by the GFZ Potsdam, the University of Potsdam, the Royal Observatorium of Belgium and NARS at the Utrecht University. This paper has been partly supported by the program "Intérieur de la Terre" of INSU (Institut National des Sciences de l'Univers). IPGP contribution 1943.

References

Andresen, B., and J. M. Gordon (1994), Constant thermodynamic speed for minimizing entropy production in thermodynamic processes and simulated annealing, *Phys. Rev. E*, *50*, 4346–4351.

Bhattacharyya, J., P. Shearer, and G. Masters (1993), Inner core attenuation from short-period *PKP*(BC) versus *PKP*(DF), *Geophys. J. Int.*, *114*, 1–11.

Bijwaard, H., W. Spakman, and E. Engdahl (1998), Closing the gap between regional and global travel time tomography, *J. Geophys. Res.*, *103*, 30,055–30,078.

Bréger, L., B. Romanowicz, and H. Tkalčić (1999), *PKP*(BC-DF) travel time residuals and short scale heterogeneity in the deep Earth, *Geophys. Res. Lett.*, *26*, 3169–3172.

Bréger, L., H. Tkalčić, and B. Romanowicz (2000), The effect of D″ on *PKP*(AB-BC) travel time residuals and possible implications for inner core structure, *Earth Planet. Sci. Lett.*, *175*, 133–143.

Chapman, C. (1978), A new method for computing synthetic seismograms, *Geophys. J. R. Astron. Soc.*, *54*, 481–518.

Chevrot, S. (2002), Optimal waveform and delay time analysis by simulated annealing, *Geophys. J. Int.*, *151*, 164–171.

Choy, G., and P. Richards (1976), Pulse distortion and Hilbert transformation in multiply reflected and refracted body waves, *Bull. Seismol. Soc. Am.*, *65*, 55–70.

Cormier, V., L. Xu, and G. Choy (1998), Seismic attenuation of the inner core: Viscoelastic or stratigraphic?, *Geophys. Res. Lett.*, *25*, 4019–4022.

Creager, K. (1992), Anisotropy of the inner core from differential travel times of the phases *PKP* and *PKIKP*, *Nature*, *356*, 309–314.

Doornbos, D. (1974), The anelasticity of the inner core, *Geophys. J. R. Astron. Soc.*, *38*, 397–415.

Doornbos, D. (1983), Observable effects of the seismic absorption band in the Earth, *Geophys. J. R. Astron. Soc.*, *75*, 693–711.

Dziewonski, A., and D. Anderson (1981), Preliminary reference Earth model, *Phys. Earth Planet. Inter.*, *25*, 297–356.

Engdahl, E., R. Van der Hilst, and R. Buland (1998), Global teleseismic earthquake relocation with improved travel times and procedures for depth determination, *Bull. Seismol. Soc. Am.*, *88*, 722–743.

Garcia, R. (2002), Constraints on upper inner core structure from waveform inversion of core phases, *Geophys. J. Int.*, *150*, 651–664.

Garcia, R., and A. Souriau (2000), Inner core anisotropy and heterogeneity level, *Geophys. Res. Lett.*, *27*, 3121–3124. (Correction to Inner core

anisotropy and heterogeneity level, *Geophys. Res. Lett.*, *28*, 85–86, 2001.)
Helffrich, G., and S. Sacks (1994), Scatter and bias in differential *PKP* travel times and implications for mantle and core phenomena, *Geophys. Res. Lett.*, *21*, 2167–2170.
Helffrich, G., S. Kaneshima, and J.-M. Kendall (2002), A local, crossing path study of attenuation and anisotropy of the inner core, *Geophys. Res. Lett.*, *29*(12), 1568, doi:10.1029/2001GL014059.
Isse, T., and I. Nakanishi (2002), Inner-core anisotropy beneath Australia and differential rotation, *Geophys. J. Int.*, *151*, 255–263.
Kárason, H., and R. Van der Hilst (2001), Tomographic imaging of the lowermost mantle with differential times of refracted and diffracted core phases (*PKP*, P_{diff}), *J. Geophys. Res.*, *106*, 6569–6587.
Kennett, B., and E. Engdahl (1991), Traveltimes for global earthquake location and phase identification, *Geophys. J. Int.*, *105*, 429–465.
Kennett, B., E. Engdahl, and R. Buland (1995), Constraints on seismic velocities in the Earth from traveltimes, *Geophys. J. Int.*, *122*, 108–124.
Kolář, P. (2000), Two attempts of study of seismic source from teleseismic data by simulated annealing non-linear inversion, *J. Seismol.*, *4*, 197–213.
Kuperman, W., M. Collins, J. Perkins, and N. Davis (1990), Optimal time-domain beamforming with simulated annealing including application of a priori information, *J. Acoust. Soc. Am.*, *88*, 1802–1810.
Luo, S.-N., S. Ni, and H. D. V. (2001), Evidence for a sharp lateral variation of velocity at the core-mantle boundary from multipathed *PKP*ab, *Earth Planet. Sci. Lett.*, *189*, 155–164.
Mooney, W., G. Laske, and G. Masters (1998), CRUST5.1: A global model at $5^\circ \times 5^\circ$, *J. Geophys. Res.*, *103*, 727–747.
Niazi, M., and L. Johnson (1992), *Q* in the inner core, *Phys. Earth Planet. Inter.*, *74*, 55–62.
Niu, F., and L. Wen (2001), Hemispherical variations in seismic velocity at the top of the Earth's inner core, *Nature*, *410*, 1081–1084.
Nulton, J., and P. Salamon (1988), Statistical mechanics of combinatorial optimization, *Phys. Rev. A*, *37*, 1351–1356.
Ritter, J., U. Achauer, U. Christensen, and Eifel Plume Team (2000), The teleseismic tomography experiment in the Eifel region, Central Europe: Design and first results, *Seismol. Res. Lett.*, *71*, 437–443.
Salamon, P., and R. Berry (1983), Thermodynamic length and dissipated availability, *Phys. Rev. Lett.*, *51*, 1127–1130.
Sen, M., and P. Stoffa (1995), *Global Optimization Methods in Geophysical Inversion*, Elsevier Sci., New York.
Sharma, S., and P. Kaikkonen (1998), Two-dimensional non-linear inversion of VLF-R data using simulated annealing, *Geophys. J. Int.*, *133*, 649–668.
Song, X. (1997), Anisotropy of the Earth's inner core, *Rev. Geophys.*, *35*, 297–313.
Souriau, A., and G. Poupinet (1991), The velocity profile at the base of the liquid core from *PKP*(BC+Cdiff) data: An argument in favour of radial inhomogeneity, *Geophys. Res. Lett.*, *18*, 2023–2026.
Souriau, A., and B. Romanowicz (1996), Anisotropy in inner core attenuation: A new type of data to constrain the nature of the solid core, *Geophys. Res. Lett.*, *23*, 1–4.
Souriau, A., and P. Roudil (1995), Attenuation in the uppermost inner core from broad-band GEOSCOPE *PKP* data, *Geophys. J. Int.*, *123*, 572–587.
Tanaka, S., and H. Hamaguchi (1997), Degree one heterogeneity and hemispherical variation of anisotropy in the inner core from *PKP*(BC)-*PKP*(DF) times, *J. Geophys. Res.*, *102*, 2925–2938.
Tkalčić, H., B. Romanowicz, and N. Houy (2002), Constraints on D" structure using *PKP*(AB-DF), *PKP*(BC-DF), and *Pc*P-P traveltime data from broad-band records, *Geophys. J. Int.*, *148*, 599–616.
VanDecar, J., and R. Crosson (1990), Determination of teleseismic relative phase arrival times using multi-channel cross-correlation and least squares, *Bull. Seismol. Soc. Am.*, *80*, 150–169.
Van der Hilst, R., S. Widiyantoro, and E. Engdahl (1997), Evidence for deep mantle circulation from global tomography, *Nature*, *386*, 578–584.

S. Chevrot, Laboratoire de Dynamique Terrestre et Planétaire, CNRS UMR5562, F-31400 Toulouse, France.
R. Garcia, Département de Géophysique Spatiale et Planétaire, IPGP, CNRS UMR7096, 4, Ave de Neptune, F-94107 Saint Maur Cedex, France. (garcia@ipgp.jussieu.fr)
M. Weber, GeoForschungsZentrum, D-14473 Potsdam, Germany.